A CUBED SPHERE GRAVITY MODEL FOR FAST ORBIT PROPAGATION

Brandon A. Jones, George H. Born,[*] **and Gregory Beylkin**[†]

The cubed sphere model of the gravity field maps the primary body to the surface of a segmented cube, with a basis defined on the cube surface for interpolation purposes. As a result, the model decreases orbit propagation time and provides a localized gravity model. This paper provides a brief description of the cubed sphere model, which is currently derived from the spherical harmonics. Early tests of the integration constant did not meet requirements, thus the model was reconfigured to improve accuracy. A detailed characterization of the model was then performed to profile agreement with the base model. The new model closely approximates the spherical harmonics with orbits deviating by a fraction of a millimeter at or above feasible Earth-centered altitudes.

INTRODUCTION

Conceptually, a sphere is a rather basic geometrical object. It is simply the collection of all points in a three dimensional space that are some distance r from the center. However, defining a basis on the surface of the sphere has not proven as simple. The method most commonly used for such objects is the spherical harmonics. In the case of geopotential, the model is

$$U\left(r, \phi, \lambda\right) = \frac{\mu}{r}\left(1 + \sum_{n=2}^{\infty}\sum_{m=0}^{n}\left(\frac{R}{r}\right)^{n}P_{n,m}\left[\sin\phi\right]\left(C_{n,m}\cos\left(m\lambda\right) + S_{n,m}\sin\left(m\lambda\right)\right)\right) \quad (1)$$

where ∇U is the resulting gravitational acceleration. The gravity model itself is described by the coefficients $C_{n,m}$ and $S_{n,m}$.

When using the spherical harmonics, model accuracy improves by increasing the model degree and order. Unfortunately, an increase in the degree and order of the model by a factor of 10 results in computation time increasing by a factor of 100.[1] Interpolation models have been developed to make evaluation faster. These models have ranged from preserving the spherical coordinate system,[2, 3] to models that more drastically reformulate the evaluation of the gravity field.[4, 5] As demand for improved gravity model accuracy increases, so do the computational resources required for model evaluation. Additionally, orbits about bodies with irregular mass distributions, such as the moon, require a high degree model to properly propagate an orbit.[6]

With the spherical harmonics, deviations from the sphere at a single point are modeled by accumulating the deviation generated by panels defined over the complete sphere. Hence each term is part of a global model. Unfortunately, the spherical harmonics model is unable to meet the demands for regional representations.[7] Several alternative methods have been explored to localize the gravity field for these scientific applications.[8, 9]

[*]Colorado Center for Astrodynamics Research, University of Colorado Boulder, 431 UCB, Boulder, CO, 80309
[†]Department of Applied Mathematics, University of Colorado Boulder, 526 UCB, Boulder, CO, 80309

A new model, the cubed sphere, was developed to localize the gravity field and decrease the model evaluation time.[1] At its core, the cubed sphere is an interpolation model that relies on a localized basis defined on the surface of a segmented cube. This cube is mapped to a sphere to represent spherical objects. This paper explores applications of this cubed sphere model to orbit propagation, particularly how it compares to the spherical harmonics model solutions.

THE CUBED SPHERE MODEL

Originally proposed by Beylkin and Cramer,[1] the cubed sphere model defines a new method to compute geopotential and acceleration. Essentially, the sphere is mapped to a cube with a new coordinate system defined on each side. Each cube panel is segmented by a uniform grid and interpolation is performed on the face to find the acceleration at that point. Multiple cubes are nested within each other and interpolation is performed between adjacent cubes to account for the acceleration variation in the radial direction. Hence, the model is described as a cubed sphere and is conceptualized by Figure 1. A grid spacing scheme is established with values for acceleration precomputed at intersections of the grid lines. Basis splines, or B-splines, were selected as the basis on each face of the cube. The next section describes the cubed sphere model in detail.
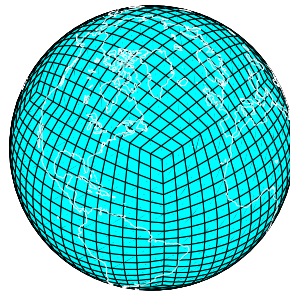

Figure 1. Illustration of the cubed sphere

The Model

The cubed sphere model may be used to approximate any number of elements defined on a primary body. For example, it can approximate each component of acceleration, or the gravity potential. The accelerations are not directly derived from potential, but stored as a separate parameter. Thus, in order for a model to provide both potential and three components of acceleration, four parameters must be stored at each point for future interpolation. In the following sections, any reference to modeling the gravity potential may also be used to model acceleration when the appropriate adjustments are made. Although the cubed sphere model is described in the literature, a more detailed description is included here to improve clarity. The design of the model described in this section was originally the work of Beylkin and Cramer.[1]

The cubed sphere model is currently derived from a given model, hereafter called the base model. Although other models such as a polyhedron or mascon may be utilized, currently the spherical harmonic model is used. The first four terms of the spherical harmonic expansion, i.e. the two-body term, J_2, the $(*)_{2,1}$, and $(*)_{2,2}$ terms are not represented by the cubed sphere model. Given the decreasing contribution of the higher order terms to the global gravity field, these lower order terms are not included in the cubed sphere model to prevent loss of accuracy due to machine precision.

The geopotential values computed by the remaining base model are then used to define the basis functions on the surface of the cube. Although other formulations are possible, B-splines are currently used. The method for deriving the cubed sphere will now be defined.

A major property of the cubed sphere model that must be defined is the grid size, N. Similar to the degree and order of the spherical harmonic model, the grid size is a measure of model fidelity and defines the density of the grid on each cube panel. For a given altitude, the values of latitude and longitude are segmented such that

$$\theta = 2\pi x, \quad \phi = 2\pi y \tag{2}$$

where x and y are discrete values in the range $[0, 1)$ with spacing N^{-1}. It may not be readily apparent why the latitude, ϕ, is in the range $[0, 2\pi)$, but this will be understood in a moment.

Latitude and longitude have been mapped to a two dimensional grid specified by x and y to solve for the B-spline interpolation scheme. As described in the appendix, the interpolation coefficients are easily derived in the Fourier domain for a periodic, two dimensional plane. If the grid variables x and y are 1-periodic, then the two-dimensional FFT algorithm may be used. The values of potential at grid intersection points are used as data values. Hence, given a cube is comprised of six planes, the FFT algorithm provides a simplified method for representing the potential on the surface of a cube.

If ϕ only varies from $-\pi/2$ to $\pi/2$, or 0 to π, then y is not 1-periodic. Thus, the formulation of the Earth's geopotential must be duplicated to complete the period. The mathematical formulation of the new geopotential, U_p, is then

$$U_p(r, \phi, \theta) = \begin{cases} U(r, \phi, \theta) & \text{if } 0 \leq \phi < \phi, \\ U(r, 2\pi - \phi, \theta + \pi) & \text{if } \pi \leq \phi < 2\pi \end{cases} \tag{3}$$

and ϕ is now a value in the range $[0, 2\pi)$ and 2π-periodic. Thus, y is now 1-periodic and the FFT algorithm is used to generate the B-spline interpolation coefficients. Note the doubling of the geopotential model is only used to generate these coefficients.

To prevent grid distortion given the ambiguity of longitude at the poles, the Earth is rotated so that the poles lie along the equator. This is equivalent to the transverse mercator map projection. A second x-y plane is generated after this rotation, with the FFT algorithm applied and a second set of B-spline coefficients determined. This rotation is performed in the formulation of the base model.

B-spline coefficients have been defined over the flat surface of the two x-y grids. The grids are then broken into appropriate segments to generate the faces of a cube. Each face, or panel, of the cube has a new x-y grid with axes defined over the range $[-1, 1]$. Four panels along the middle latitudes are selected from the first plane, while the two remaining panels along the poles are selected from the second plane. Grid spacing is preserved along the face of the cube, however the new panels are a quarter of the size. Thus, the size of the grid on each panel is $N/4$ by $N/4$. This property is used in the naming convention defined for a given model. A CS-X model is a cubed sphere model where X corresponds to the grid size on a cube face, or $N/4$. Finally, the geopotential model for the given shell has now been defined and is represented as a cube.

Additionally, a user specified number of nested, concentric shells is defined for interpolation in the radial direction. Shell spacing is determined by defining a set number of points (h_j) equally

spaced in the interval $[0, 1]$. Shell locations are then

$$\frac{R}{r_j} = 1 - h_j^2 \qquad (4)$$

where r_j is the radial distance of the shell. These ratios, which represent a distance above the planet's surface in the range $(0, 1]$, define shell locations. As the ratio approaches zero, the orbit radius approaches infinity. Shell density increases as altitude decreases, corresponding to the inverse square relationship between geopotential and radius. The final shell at a radius of infinity is not computed. The model assumes eventual decay to zero of the spherical harmonic terms, thus the two-body equation will govern satellite dynamics.

These primary shells are modeled with each consisting of subshells for polynomial interpolation of a prescribed degree in the radial direction. For a fifth degree interpolation scheme, six subshells are required. The spacing between subshells is mapped to the range $[-1, 1]$ where zero corresponds to the midpoint between primary shells. The subshells are then located at the Chebyshev nodes based on the degree of the polynomial. Chebyshev nodes were selected to minimize interpolation error due to node selection. Each primary and subshell is independent of all others, thus there is no coupling in model generation. B-spline coefficients for each shell are generated as previously described using the applicable altitude for the evaluation of Eq. 3. A total of $(l + 1) \times M$ shells are computed where l is the degree of the interpolating polynomial and M is the number of primary shells. It is important to note the mapping to the cube is simply used for data storage and solving for the spline coefficients. All parameters described by the model, more specifically components of acceleration, are still represented in the spherical coordinate system. The cube provides a uniform grid for B-spline coefficient determination and a data structure for faster computation.

Implementation of the cubed sphere model is rather straightforward. The point of interest is mapped to the cube, and interpolation along the face and between shells is performed to determine the higher degree acceleration. Lower degree accelerations are computed using the spherical harmonic coefficients stored in the model. The conversion from spherical (ϕ, λ) to cube coordinates (x, y, n) is summarized in Table 1, and was adapted from Beylkin and Cramer.[1] For the cube coordinates, n refers to the face of the cube. The first four panels represent the sphere at the middle latitudes between -45° and 45°, while panels 5 and 6 correspond to the polar regions.

Table 1   Spherical to rectangular coordinates conversion. Note $\gamma = \cos\phi\sin\theta$, $\omega = \tan\phi/\cos\theta$, and $\alpha = 4/\pi$.

Face	Angle Ranges	X-coordinate	Y-coordinate
1	$-\pi \leq \theta < -\pi/2, \quad -\pi/4 \leq \phi \leq \pi/4$	$\alpha\theta + 3$	$\alpha\phi$
2	$-\pi/2 \leq \theta < 0, \quad -\pi/4 \leq \phi \leq \pi/4$	$\alpha\theta + 1$	$\alpha\phi$
3	$0 \leq \theta < \pi/2, \quad -\pi/4 \leq \phi \leq \pi/4$	$\alpha\theta - 1$	$\alpha\phi$
4	$\pi/2 \leq \theta < \pi, \quad -\pi/4 \leq \phi \leq \pi/4$	$\alpha\theta - 3$	$\alpha\phi$
5	$|\gamma| \leq 1, |\omega| \geq 1, \phi > 0$	$\alpha\tan^{-1}(\omega) \pm 2$	$\alpha\sin^{-1}(\gamma)$
6	$|\gamma| \leq 1, |\omega| \geq 1, \phi < 0$	$\alpha\tan^{-1}(\omega) \pm 2$	$\alpha\sin^{-1}(\gamma)$

Model Configuration

Test software was written to evaluate the model at a user defined number of random points above the primary body. For each point, the cubed sphere model is compared to the base model and the L_∞ norm is evaluated. The maximum norm of all points is then used to characterize the accuracy of the model. Tests utilized 10^5 random points, with any increases yielding similar results. The original cubed sphere model differed from the spherical harmonics by as much as 10^{-9} m/sec^2. Although this value may appear rather small, the model was reconfigured and accuracy was improved to 10^{-11} m/sec^2, and 10^{-14} m/sec^2 for lower fidelity models. The main focus of this reconfiguration was to improve model performance for higher fidelity models, i.e. equivalents to the 70x70 models and those of higher degree and order. Full benefits of the reconfiguration will be demonstrated in the section discussing the integration constant performance.

Table 2. Cubed Sphere Configuration

Property		Before	Current
Number of parameters estimated (P)		3	4
B-spline degree (m)		11	11
Chebyshev polynomial degree (l)		5	11
Number of primary shells (M)		13	13
	CS-30 / 20x20	80	120
Grid Density (N) for:	CS-76 / 70x70	280	304
	CS-162 / 150x150	600	648

Changes to the cubed sphere configuration made in the course of this research, along with other major properties, are included in Table 2. Note the change in Chebyshev polynomial degree and grid density did result in a file size increase. Additionally, the original model did not include the estimate of the potential at a given point. Of course, these configuration parameters can be tailored to a specific design based on orbit accuracy requirements and file size limitations. If the potential is not required, the file size is reduced by almost 25%. Table 2 defines the base models for the CS-30, CS-76, and CS-162 models used throughout this study. Other changes were made to the software to improve computation speed and switch from the unnormalized to normalized formulation of the associated Legendre functions in the base model. Finally, the model storage scheme of the B-spline coefficients was altered to allow for loading of selected shells to reduce software memory requirements and decrease initialization time.

The number of elements that must be stored in the model are computed using

$$Number\ of\ elements = 6P(l+1)M\left(\frac{N}{4}+m\right)^2 \tag{5}$$

where the meaning of the terms are found in Table 2 or the notation section. Additionally, there is some memory overhead associated with the file header. For the CS-30 model, this results in a 49 Mb file. Similarly, a 856 Mb file is required for a CS-162 model. However, the complete model is not required for most applications. Since the model is localized, only the primary and secondary shells required for a given orbit must be generated or loaded into memory.

5

Experimental results demonstrate the evaluation time of the cubed sphere model is slightly more than the 20x20 spherical harmonics. As the model grid density is increased, corresponding to an increase in model fidelity, evaluation time does not increase. The B-spline coefficients are organized such that no search is necessary. If the degree of the interpolating functions remains constant for each grid size, model evaluation time remains constant. Thus, speed-up factors compared to the spherical harmonics increases with model fidelity.

COMPARISONS TO THE SPHERICAL HARMONICS MODEL

After the cubed sphere was fully developed, it was compared to the spherical harmonics model. The GGM02C[10] model was selected as both the base model of the cubed sphere and the basis of comparison for the following tests. Evaluations included a comparison of the integration constant, spatial comparisons of the models in the form of gravity anomaly plots, and finally the propagated orbits themselves.

The TurboProp orbit integration package[11] was used to minimize software development time. This software provides integration tools implemented in C that are compatible with MATLAB. Unreleased versions are also compatible with Python. The cubed sphere model, along with the necessary interface code, was implemented within the TurboProp framework. However, the software can be easily ported to other packages. For the following tests requiring orbit propagation, the TurboProp Runge Kutta 7(8) integrator was used to simplify integrator setup with automated execution for a variety of initial conditions. Other integrators were tested, including symplectic Runge Kutta algorithms, but yielded similar results. The absolute integration tolerance was set to 10^{-12}.

Orbits were propagated for 24 hours with a variety of initial conditions and states output every 20 seconds. The initial orbit altitude was varied between 100 and 1,000 km at 50 km intervals. Model accuracy relative to the spherical harmonics decreases with reductions in altitude, however most satellites orbit at or above 300 km. Thus, altitude specific results in the following sections are provided at 300 km. The right ascension of the ascending node (Ω) ranged from $0°$ to $180°$ in $5°$ increments, while the inclination varied from and $0°$ to $85°$ in $2.5°$ intervals. All other orbit elements were initially set to zero. The inclination was intentionally kept below $85°$ to avoid the singularity at the poles in the classical formulation of the spherical harmonics. Thus, for each altitude, 1,295 orbits were tested. The Greenwich sidereal time was set to $0°$ at the epoch time, with an Earth rotation rate of $360°$ per solar day. The planetary radius and gravitation parameter were set to the appropriate value as determined by the base model. Each set of initial conditions was propagated using the cubed sphere and the corresponding base model. The trajectories were differenced and 3D RMS differences were calculated and stored. Any reference to an orbit propagation "error" is defined as the difference between the cubed sphere and the spherical harmonic model orbits. The three models described in Table 2 were tested.

Integration (Jacobi) Constant Comparisons

A given geopotential model must satisfy the Laplace equation,

$$\nabla^2 U = \frac{\partial^2 U}{\partial x^2} + \frac{\partial^2 U}{\partial y^2} + \frac{\partial^2 U}{\partial z^2} = 0 \tag{6}$$

Unfortunately, there is no direct method to calculate the second derivatives of the cubed sphere. Parameters could be added to the model to estimate these values, similar to the those modeling

the geopotential and the gravity accelerations. However, this will drastically increase file size. Additionally, finite differencing would only be an approximation.

Instead of testing the cubed sphere under the Laplace criterion, another technique using the Jacobi-like integration constant,[12]

$$K = \frac{\dot{\vec{r}} \cdot \dot{\vec{r}}}{2} - \left[\frac{\mu}{r} - U(\vec{r}, t)\right] - \vec{\omega} \cdot (\vec{r} \times \dot{\vec{r}}) \tag{7}$$

is used. This constant assumes the geopotential is a time varying potential, which is valid due to Earth rotation. Here, $\vec{\omega}$ is the angular velocity of the primary body. For a valid gravity model and a propagated orbit, K must remain constant over time, or $K - K_\circ$ equals zero. In practice, the constant fluctuates due to the numerical integration process and errors in the estimate of the gravity field.
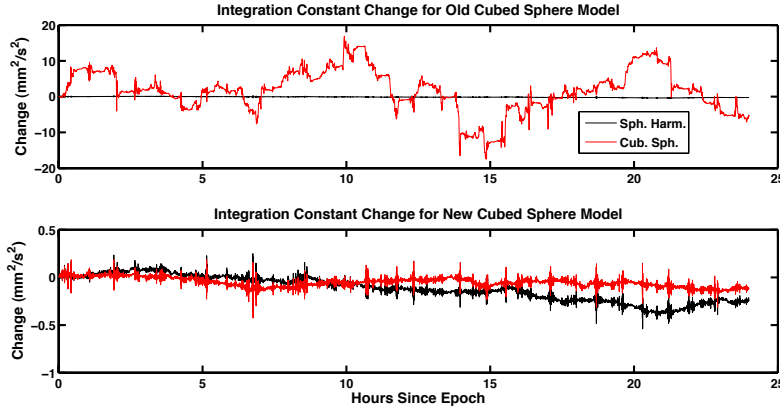
Figure 2 **Changes in integration constant with the new CS-162 model configuration for an orbit with an inclination of $15°$ and right ascension of $50°$ at a 300 km altitude.**

As mentioned previously, the cubed sphere was reconfigured to improve accuracy. The principle motivation for this alteration was improving the integration constant performance. Figure 2 illustrates the extent of the improvement. Previously, the cubed sphere integration constant was consistently 1-3 orders of magnitude greater. This result would reduce the validity of the model for applications requiring long term orbit propagation, thus the model was reconfigured. In some cases, such as this example, the integration constant performs better than the spherical harmonics with the new configuration.

Table 3. Fraction of runs where $O(K-K_\circ)$ is less than the other model.

Model	Cubed Sphere	Spherical Harmonics
CS-30	0.024%	0.020%
CS-76	0.012%	0.008%
CS-162	0.264%	0.272%

A major concern when comparing the variations in the integration constant for the cubed sphere and the spherical harmonics models is the relative magnitude of the fluctuations. In some cases, the

magnitude of the variations of the cubed sphere were as much as an order of magnitude less than the spherical harmonics, and vice versa. Table 3 provides the percentage of the 24,605 runs for each model that exhibited this behavior. In most cases, the order of magnitude of the fluctuations was the same. However, a small percentage of the tests yielded integration constant changes an order of magnitude less for one model when compared to the other. In the case of the CS-162 model, where the percentage of runs sharply increased, tests at altitudes at or below 250 km exhibited the larger fluctuations.
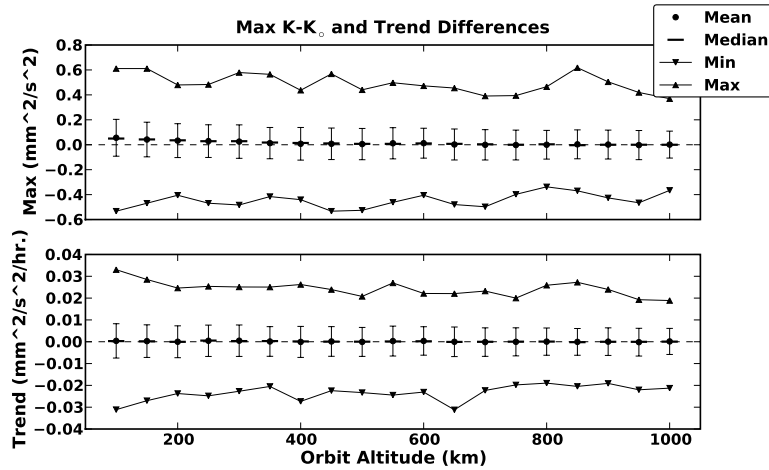
Figure 3 Comparison of the integration constant variations for the CS-30 model with the spherical harmonics base model. Error bars are 1-σ.

In addition to the magnitude of the variations, any trends in the integration constant variations should be considered. For a given orbit, the maximum of the absolute values of the fluctuations for the cubed sphere and the spherical harmonics were differenced. Similarly, a linear fit was performed on the integration constant change for a single orbit and the differences in the absolute values of the slopes for the models were calculated. Statistics were assembled on the model performance for each altitude, with the results provided in Figure 3 for the CS-30 model. In both cases, a negative number means the cubed sphere model exhibited smaller variations or trends in the integration constant. For the slope in the trend line, units are designated as $mm^2/sec^2/hour$. Since the units of the integration constant are mm^2/sec^2, the mixture of seconds and hours is intended to preserve the change of the integration constant over a given time period. For altitudes below 400 km, the mean and median magnitude differences indicate the spherical harmonics model slightly outperforms the cubed sphere. However, the average difference drops to nearly zero above 400 km. The maximum and minimum differences remain consistent. Given the mean and median differences in the trend line slope are around zero with 1-σ values within 0.01 $mm^2/sec^2/hour$, the two models typically have the same long term trend.

Figure 4 illustrates the integration constant performance for the CS-76 model. Note the magnitude and trend of the integration constant change is larger for the cubed sphere at lower altitudes, but settles at around 300 km. The median is smaller than the mean at these lower altitudes, indicating a relatively small number of tests increase the mean value. Again, the models closely agree for higher altitudes, as indicated by the mean and median values with small error bars.
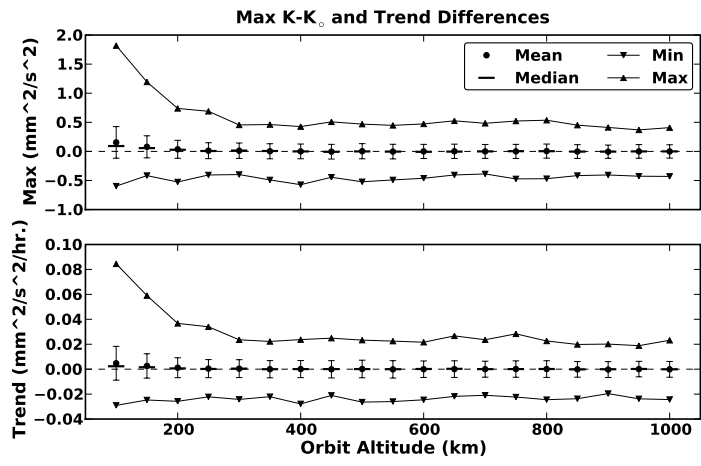
8

Figure 4 **Comparison of the integration constant variations for the CS-70 model with the spherical harmonics base model. Error bars are 1-σ.**
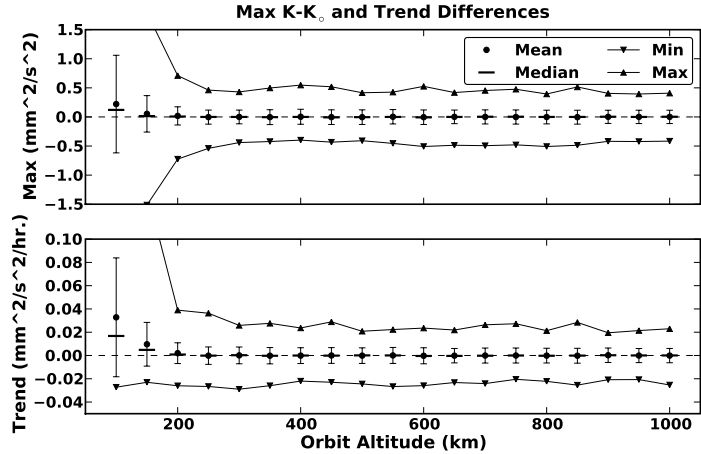

Figure 5 **Comparison of the integration constant variations for the CS-150 model with the spherical harmonics base model. Error bars are 1-σ.**

Results for the CS-162 model are provided in Figure 5. Note some extreme values have been truncated to improve visibility of performance statistics at higher altitudes. In the case of the differences in the magnitude differences, the minimum values for the 100 and 150 km orbits are -3.39 and -1.51 mm^2/sec^2, respectively. The maximum values are 5.20 and 1.79 mm^2/sec^2. In the case of the trend slope differences, the missing maximums are 0.44 and 0.14 $mm^2/sec^2/hour$. Like the CS-76 model, differences between the cubed sphere and spherical harmonics models are greater at lower altitudes. This trend remains consistent through the remaining tests, and is attributed to the greater differences in the gravity anomalies at lower altitudes seen in the next section. In this case, the differences in the models settles around 250 km.

Gravity Anomaly Comparisons

In this section, a spatial comparison of the differences in the modeled accelerations is provided. The results are represented in gravity anomaly plots projected onto the surface of the Earth. The acceleration vector was evaluated at a common altitude with latitude and longitude varied in $0.5°$ intervals. The magnitude of the differences in the vector is then illustrated. Like the orbit propagation tests, acceleration vectors were not computed at the poles to avoid the singularity in the spherical harmonics model.
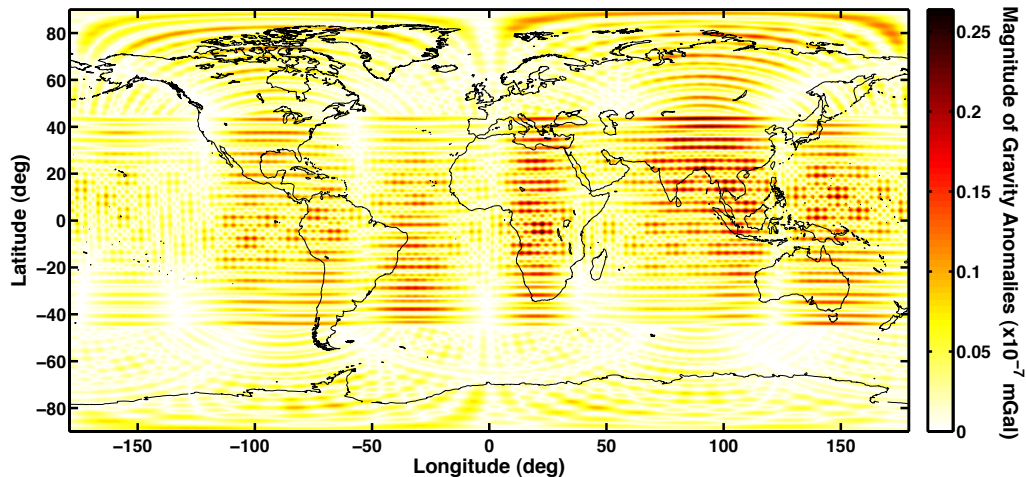
Figure 6. CS-30 gravity anomalies at 300 km

The gravity anomalies for the CS-20 model at an altitude of 300 km are provided in Figure 6, and demonstrate anomalies are less than 10^{-7} mGal. The cube grid is visible in the variations in the anomalies, especially over the East Indies. The regions of peak variation correspond to regions of high gravity fluctuations, as determined by the spherical harmonics model. For example, the Himalayan mountain ranges and the East Indies.

The gravity anomalies for the CS-162 model at 300 km are found in Figure 7. The grid spacing is still visible, but areas of peak variations are isolated to select regions. Like the previous cases, these regions correspond to those with a generally large variation in the gravity field. The magnitude of the anomalies is again on the order of 10^{-8} mGal, with the largest anomaly off of the coast of Haiti at approximately $18°$ latitude and $-67°$ longitude. Gravity anomalies for the CS-76 model are not
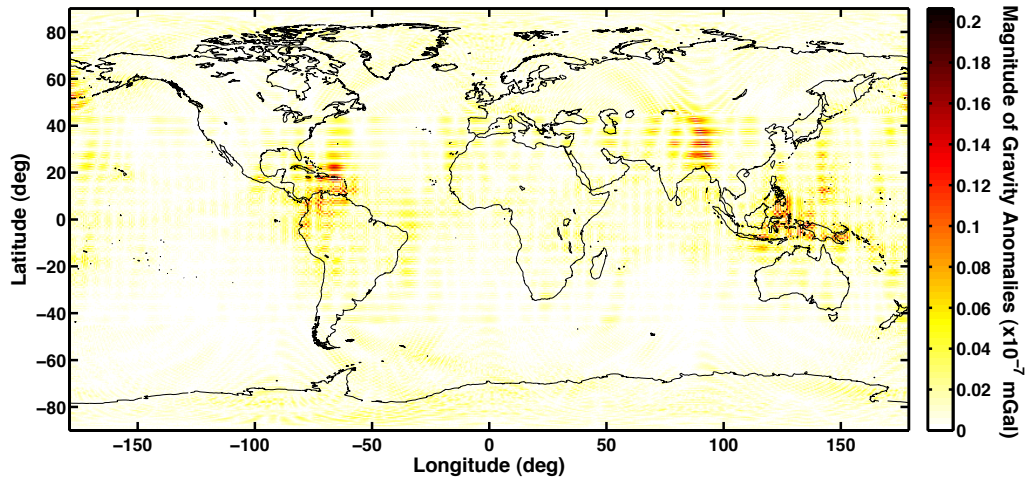
Figure 7. CS-162 gravity anomalies at 300 km

included, but yielded similar results to the previous two models. The grid spacing was visible, but the regions of higher differences were not as isolated as the CS-162 case.
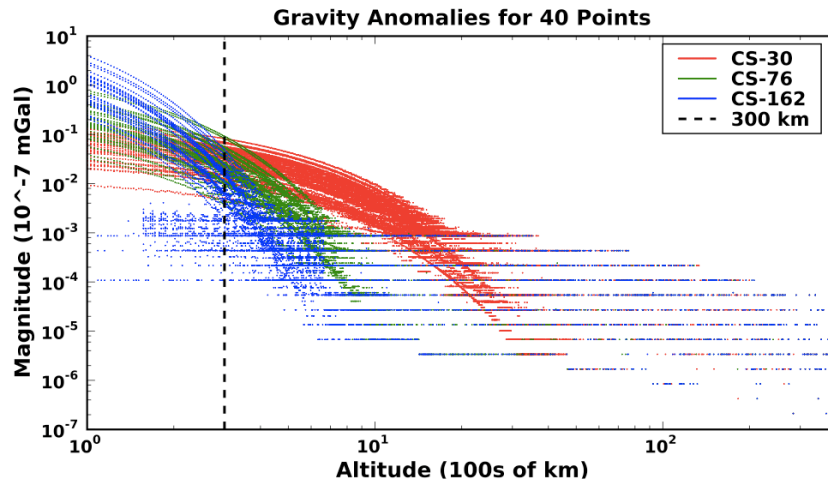

Figure 8   Variations in gravity anomalies with altitude for 42 points on the Earth using the CS-30, CS-76, and CS-162 models.

To illustrate gravity anomaly variations with altitude, Figure 8 illustrates the difference in gravity anomalies for each of the models for altitudes up to geosynchronous orbit. Most of the forty points depicted were randomly selected, although a couple of points were chosen to coincide with regions of expectedly large anomalies, such as the Himalayan mountains. As expected, peak variations in the cubed sphere model with respect to the spherical harmonics occur at lower altitudes. Additionally, the largest anomalies occur for the higher fidelity models. At various altitudes, the differences become discretized due to machine precision and the relatively low contribution the perturbations

11

modeled by the cubed sphere have on the overall gravity acceleration.

For the CS-162 model, there is a region below 300 km and around 10^{-10} mGal where the variations are periodic. In this case, the difference is close to the machine precision and is not determined by the grid spacing. Given the Chebyshev interpolation between shells, approximation error will vary based on proximity to the nearby shells. Thus, as the altitude increases for this point in Figure 8, the error periodically increases and decreases.

Orbit Propagation Comparisons

A summary of the orbit propagation results are found in Figure 9 for the CS-30, CS-76, and CS-162 cubed sphere models. These 3D RMS values include the state differences at all times and orbits, independent of the orbit initial conditions. Orbit position and velocity differences are on the order of fractions of a mm and mm/sec, respectively. The magnitude of the orbit propagation errors for the three models converges at 200 km, and continues with a slight downward trend as orbit altitude increases. Model performance improves with reduced fidelity at lower altitudes, which is consistent with the gravity anomalies provided in Figure 8. Of course, these results can be adjusted by the configuration of the cubed sphere. However, this demonstrates that very close agreement with the base model may be achieved.
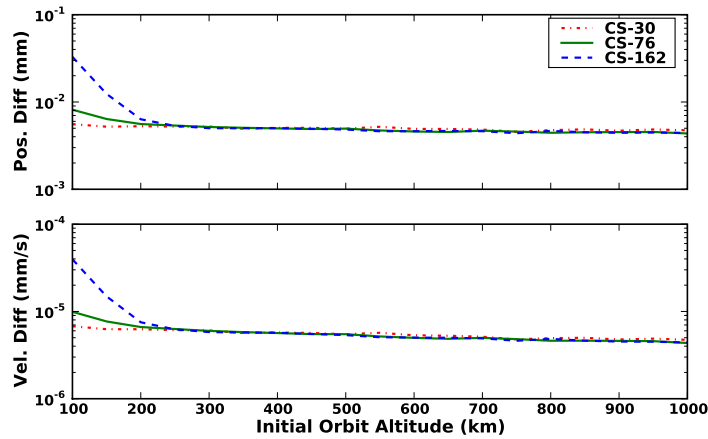

Figure 9 Summary of the total 3D RMS orbit propagation differences for the CS-30, CS-76 and CS-162 models at a given initial altitude.

**Table 4. Average Speed-Up Factor for the Cubed Sphere Versus the Base Model**

Cubed Sphere Model	Spherical Harmonics Model	Average Speed-Up Factor
CS-30	20x20	0.89
CS-76	70x70	7.13
CS-162	150x150	40.77

The ratio of the time required to propagate the orbit using the spherical harmonics and the cubed sphere were also computed. The computation time used in these calculations only included the

execution of the RK78 algorithm, and did not include file load times or software initialization. As expected, the file load time for the cubed sphere is longer than the spherical harmonics, however this can be mitigated through implementation. The speed-up factors are given in Table 4. After the model reconfiguration, specifically the increase in the degree of the polynomial interpolation between shells, the evaluation time of the model increased. Hence, the spherical harmonics is slightly faster for models of degree 20 and lower. Thus, research into altering the configuration of the lower fidelity models, specifically reducing the polynomial degree to reduce computation time, is planned.
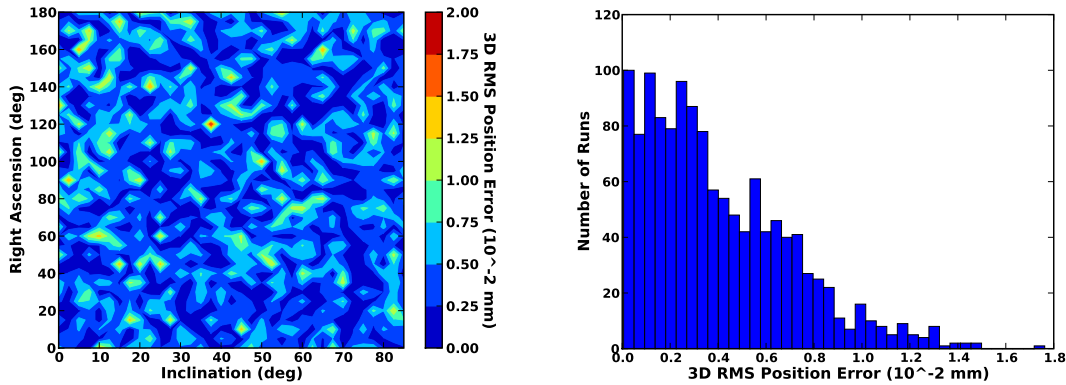

Figure 10 Spatial distribution and histogram of the 3D RMS position differences for propagated orbits initially at 300 km with the CS-162 model.
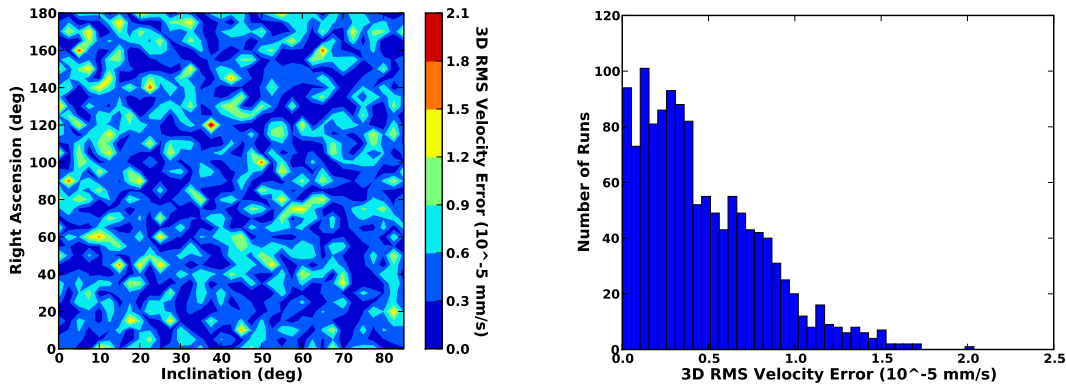

Figure 11 Spatial distribution and histogram of the 3D RMS velocity differences for propagated orbits initially at 300 km with the CS-162 model.

Orbit propagation performance specific to the CS-162 model at 300 km is illustrated in Figures 10 and 11. The minimum orbit 3D RMS was 5.71×10^{-5} mm, with a maximum of 0.0176 mm and a median of 0.0033 mm. There does not appear to be any trends in the errors when looking at their distribution based on inclination and Ω. The relatively large deviation at the Ω and inclination combination of 130° and 37.5° is directly correlated with gravity anomalies in Figure 7. Specifically, the orbit groundtrack intersects the large anomalies at approximately 28° latitude and 92° longitude twice during the orbit, and once directly over the peak anomaly near Haiti. Other than this orbit,

13

all others are within 0.015 mm of the spherical harmonics. The spatial distribution of the velocity errors roughly corresponds to the position errors, with a minimum of 2.503×10^{-8} mm/sec and a maximum of 2.037×10^{-5} mm/sec. The median 3D RMS velocity error was 3.80×10^{-6} mm/sec.
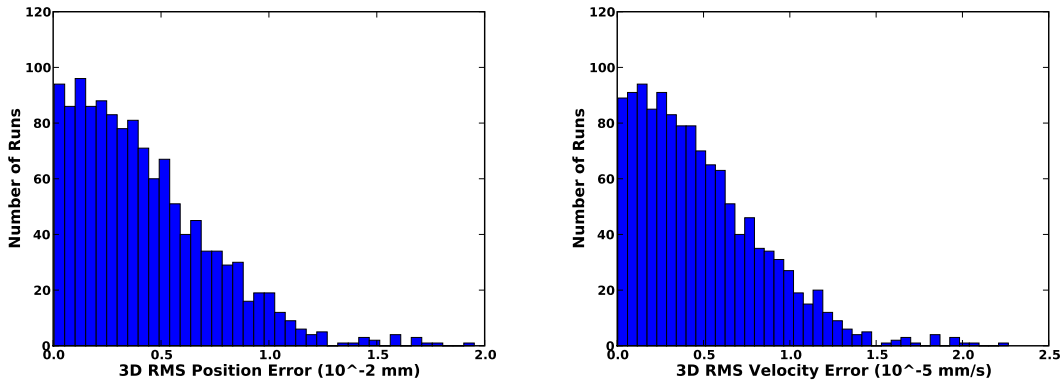
Figure 12   Distribution of 3D RMS differences for propagated orbits initially at 300 km with the CS-30 model.
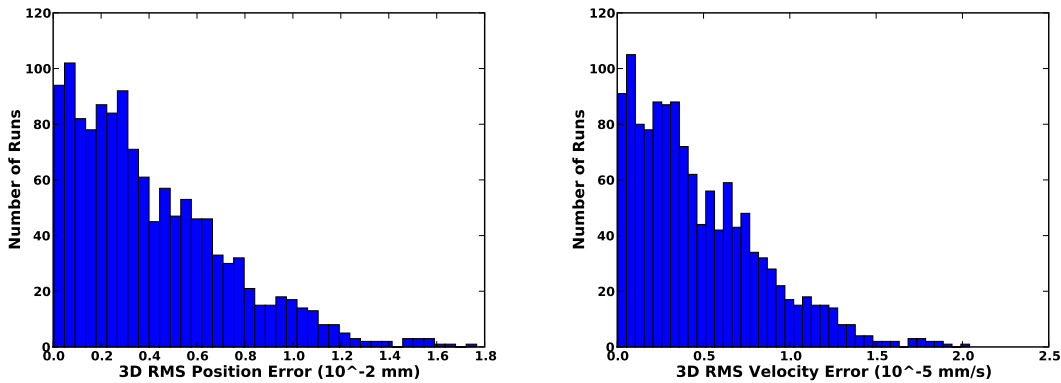
Figure 13   Distribution of 3D RMS differences for propagated orbits initially at 300 km with the CS-76 model.

Histograms of the propagation state errors for the CS-30 and CS-76 models at 300 km are provided in Figures 12 and 13, respectively. Contour plots of these errors for the CS-30 and CS-76 model have not been included since results were similar to those seen for the CS-162 model. Any accuracy differences in the results are visible in the histogram plots.

The CS-30 model position 3D RMS errors were within 0.02 mm, and as small as 4.701×10^{-5} mm. The median value was 0.0036 mm. The velocity errors had a median of 4.11×10^{-6} mm/sec, and ranged between 2.993×10^{-8} and 2.266×10^{-5} mm/sec. These results were roughly the same as those for the CS-162 model. Only twenty orbits had 3D RMS position errors above 0.0125 mm, and 17 had velocity errors above 1.5×10^{-5} mm/sec.

Orbit propagation differences for the CS-76 model were roughly the same as those of the previous two models. The minimum 3D RMS error was 3.246×10^{-5} mm, with a maximum of 0.0177 mm.

14

The median was 0.0033 mm. The velocity errors were less than 2.042×10^{-5} mm/sec, with a median of 3.788×10^{-6} mm/sec. The minimum error was 2.042×10^{-8} mm/sec.

CONCLUSIONS

Results demonstrate that the cubed sphere model closely approximates the base model, in this case the spherical harmonics. Orbit propagation tests demonstrated model agreements on the order of fractions of a millimeter, and position results are summarized in Table 5. The cubed sphere model equivalent to a 150x150 spherical harmonics was over 40 times faster. However, the spherical harmonics was slightly faster for the lower fidelity model. Future research will seek to further customize the model to improve computation efficiency for these lower fidelity models.

Table 5. Cubed Sphere Position 3D RMS Performance at 300 km

Model	Min (nm)	Max (mm)	Mean (mm)	Median (mm)
CS-30	47.0	0.0200	0.0042	0.0031
CS-76	32.5	0.0177	0.0041	0.0033
CS-162	57.1	0.0176	0.0040	0.0033

The new configuration of the cubed sphere demonstrated model improvement. Fluctuations in the integration constant were greatly reduced, with less than 1% of the orbits tested exhibiting fluctuations that differed by more than an order of magnitude between the cubed sphere and the spherical harmonics model. Changes in the integration constant, including the maximum fluctuation for a given orbit and the long term trend, are consistent between the two models. For the higher fidelity models, performance is reduced below 200 km. In some cases, the cubed sphere performs better than the spherical harmonics, probably due to slight smoothing of the model when interpolating between the nodes on the surface of the cube. Gravity anomalies were also reduced, and are now within 10^{-6} mGal for all altitudes above the Earth, and less less than 10^{-7} mGal for altitudes at or above 300 km.

Future research will include integrating the cubed sphere with the orbit determination process for both Earth and Moon based missions. Even though second derivatives currently are not included in the cubed sphere, integration with nonlinear filters, such as the unscented Kalman,[13] is rather straightforward.

Unfortunately, characterizations of moon based models were not included here. Due to the relatively extreme gravity variations due to mass concentrations caused by asteroid impacts,[6] initial results demonstrated that additional tuning of the cubed sphere for lunar applications is required. Additionally, lower altitude orbits are desirable at the moon. This is a small concern considering the cubed sphere exhibited reduced performance below 300 km. However when the ratio of the primary body radius to the orbit radius is considered, 300 km is equivalent to an 82 km altitude lunar orbit. Some additional tuning is required to improve model performance at the minimum desired altitude of 50 km at the moon.

ACKNOWLEDGMENTS

NOTATION

U	geopotential
μ	gravitational parameter (km^3/sec^2)
$\vec{r}, r$	position vector and magnitude for the satellite (km)
ϕ	geocentric latitude (rad)
λ	longitude (rad)
R	equatorial radius of the primary body
n	spherical harmonics model degree
m	spherical harmonics model order
$P_{n,m}$	associated Legendre function of x with degree and order m and n
$C_{n,m}$	cosine coefficient of spherical harmonics
$S_{n,m}$	sine coefficient of spherical harmonics
N	number of lines used to segment a plane
P	number of cubed sphere parameters estimated
l	Chebyshev polynomial degree
M	number of primary shells in cubed sphere
Ω	right ascension of the ascending node
i	inclination
K	Jacobi like integration constant
$\vec{\omega}$	primary body rotation vector
B_m	B-spline of degree m
L_m	interpolating spline of degree m
α	B-spline interpolation coefficient
$g(x)$	generic continuous function

REFERENCES

[1] G. Beylkin and R. Cramer, "Toward Multiresolution Estimation and Efficient Representation of Gravitational Fields," *Celestial Mechanics and Dynamical Astronomy*, Vol. 84, 2002, pp. 87–104.

[2] J. L. Junkins, "Investigation of Finite-Element Representations of the Geopotential," *AIAA Journal*, Vol. 14, June 1976, pp. 801–808.

[3] R. C. Engels and J. L. Junkins, "Local Representation of the Geopotential by Weighted Orthonormal Polynomials," *Journal of Guidance and Control*, Vol. 3, Jan.-Feb. 1980, pp. 55–61.

[4] A. Colombi, A. N. Hirani, and B. F. Villac, "Adaptive Gravitational Force Representation for Fast Trajectory Propagation Near Small Bodies," *Journal of Guidance, Control, and Dynamics*, Vol. 31, July-August 2008, pp. 1041–1051.

[5] R. Hujsak, "Gravity Acceleration Approximation Functions," *Advances in the Astronautical Sciences*, Vol. 93, No. Pt. 1, 1996, pp. 335–349.

[6] A. S. Konopliv, S. W. Asmar, E. Carranza, W. Sjogren, and D. Yuan, "Recent Gravity Models as a Result of the Lunar Prospector Mission," *Icarus*, Vol. 150, No. 1, 2001, pp. 1–18.

[7] M. Schmidt, M. Fengler, T.Mayer-Gurr, A. Eicker, J. Kusche, L. Sanchez, and S. Han, "Regional gravity modeling in terms of spherical base functions," *Journal of Geodesy*, Vol. 81, 2007, pp. 17–38.

[8] M. J. Fengler, D. Michel, and V. Michel, "Harmonic spline-wavelets on the 3-dimensional ball and their application to the reconstruction of the Earth's density distribution from gravitational data at arbitrarily shaped satellite orbits," *ZAMM - Journal of Applied Mathematics and Mechanics*, Vol. 86, November 2006, pp. 856–873.

[9] R. Mautz, B. Schaffrin, C. K. Shum, and S.-C. Han, *Earth observation with CHAMP, results from three years in orbit*, ch. Regional Geoid Undulations from CHAMP, Represented by Locally Supported Basis Functions, pp. 230–236. Berlin Heidelberg New York: Springer, 2004.

[10] B. Tapley, J. Ries, S. Bettadpur, D. Chambers, M. Cheng, F. Condi, B. Gunter, Z. Kang, P. Nagel, R. Pastor, T. Pekker, S. Poole, and F. Wang, "GGM02 - An Improved Earth Gravity Field Model from GRACE," *Journal of Geodesy, DOI 10.1007/s00190-005-0480-z*, 2005.

[11] K. Hill and B. A. Jones, *TurboProp Version 3.3*. Colorado Center for Astrodynamics Research, http://ccar.colorado.edu/geryon/software.html, September 2008.

[12] V. R. Bond and M. C. Allman, *Modern Astrodynamics*. Princeton, New Jersey: Princeton University Press, 1996.

[13] S. J. Julier and J. K. Uhlmann, "A New Extension of the Kalman Filter to Nonlinear Systems," *Proceedings of SPIE*, Vol. 3068, 1997, pp. 182–193.

[14] C. K. Chui, *An Introduction to Wavelets*, Vol. One of *Wavelet Analysis and Its Applications*. Boston: Academic Press, Inc., first ed., 1992.

APPENDIX: BASIS SPLINES

A simple way to introduce basis splines (or B-splines) is to define them as

$$B_m(x) = (B_{m-1} * B_0)(x), \tag{8}$$

where

$$B_0(x) = \begin{cases} 1, & |x| \leq \frac{1}{2} \\ 0, & \text{otherwise.} \end{cases} \tag{9}$$

Thus, B_m is a piecewise polynomial of degree m. On taking the Fourier transform of B_0,

$$\int_{-\infty}^{+\infty} B_0(x) e^{-2\pi i x \xi} dx = \frac{\sin \pi \xi}{\pi \xi}, \tag{10}$$

we obtain

$$\int_{\infty}^{+\infty} B_m(x) e^{-2\pi i x \xi} dx = \left(\frac{\sin \pi \xi}{\pi \xi} \right)^{m+1}. \tag{11}$$

We only consider B-splines of odd degree and note that in such case the mth degree B-spline is nonzero only in the interval $[-(m+1)/2, (m+1)/2]$. For our purposes, we use a periodized version of B-splines on the interval $[0,1]$. Subdividing $[0,1]$ into $N = 2^k$ subintervals, where $N \geq m+1$ (in practice $N \gg m+1$), we consider the basis of B-splines on this subdivision,

$$\{B_m(Nx - j)\}_{j=0,1,\ldots,2^k-1} .$$

Let us consider a function $g(x)$ that may be written as

$$g(x) = \sum_{j=0}^{N-1} \alpha_j B_m(Nx - j). \tag{12}$$

Instead of using the basis of B-splines, we may also write the same function as

$$g(x) = \sum_{j=0}^{N-1} \gamma_j L_m(Nx - j) \tag{13}$$

where L_m are interpolating splines, i.e.

$$L_m(l) = \delta_{l,0}, \tag{14}$$

where l is an integer. The definition of interpolating splines implies that the coefficients in Eq. 13 are, in fact, the values of the function $g(x)$ on the lattice,

$$g(l/N) = \gamma_l. \tag{15}$$

In our problem, we are given the values $\gamma_l = g(l/N)$ and need to find the coefficients α_j in Eq. 12. We have

$$\int_0^1 B_m(Nx - j)e^{-2\pi ixn}dx = \frac{1}{N}\hat{B}_m\left(\frac{n}{N}\right)e^{-2\pi ijn/N}, \tag{16}$$

and computing the Fourier coefficients of g in Eq. 12, we obtain

$$\hat{g}_n = \left(\frac{1}{N}\sum_{j=0}^{N-1}\alpha_j e^{-2\pi ijn/N}\right)\hat{B}_m\left(\frac{n}{N}\right) = \hat{\alpha}_n\hat{B}_m\left(\frac{n}{N}\right). \tag{17}$$

Similarly, we compute the Fourier coefficients of g in terms of interpolating splines,

$$\hat{g}_n = \left(\frac{1}{N}\sum_{j=0}^{N-1}\gamma_j e^{-2\pi ijn/N}\right)\hat{L}_m\left(\frac{n}{N}\right) = \hat{\gamma}_n\hat{L}_m\left(\frac{n}{N}\right). \tag{18}$$

The B-splines and the interpolating splines are related by (see e.g. Chui[14])

$$\hat{L}_m\left(\frac{n}{N}\right) = \frac{\hat{B}_m\left(\frac{n}{N}\right)}{a\left(\frac{n}{N}\right)} \tag{19}$$

where

$$a(\omega) = \sum_{j\in\mathbb{Z}}\left|\hat{B}_m(\omega + j)\right|^2. \tag{20}$$

It may be shown that that a is a trigonometric polynomial (see e.g. Chui[14])

$$\sum_{j\in\mathbb{Z}}\left|\hat{B}_m(\omega + j)\right|^2 = \sum_{l=-m}^{m}B_{2m+1}(l)e^{-2\pi il\omega}, \tag{21}$$

thus simplifying the evaluation of a. Finally, substituting Eq. 19 into Eq. 18, we get

$$\hat{g}_n = \hat{\gamma}_n\frac{\hat{B}_m\left(\frac{n}{N}\right)}{a\left(\frac{n}{N}\right)}, \tag{22}$$

which implies

$$\hat{\alpha}_n = \frac{\hat{\gamma}_n}{a\left(\frac{n}{N}\right)}. \tag{23}$$

In other words, applying the discrete Fourier transform to the data values $g(l/N) = \gamma_l$, scaling by the factor $1/a\left(\frac{n}{N}\right)$ and applying the inverse discrete Fourier transform, we obtain the coefficients α_j in Eq. 12. The two dimensional case is a straightforward extension, where

$$\hat{\alpha}_{k,l} = \frac{\hat{\gamma}_{k,l}}{a\left(\frac{k}{N}\right)a\left(\frac{l}{N}\right)}. \tag{24}$$